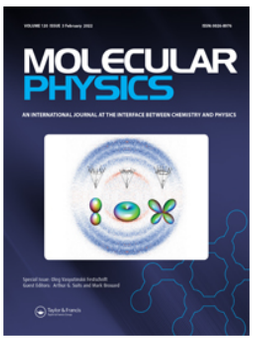

Taylor & Francis
Taylor & Francis Group

Molecular Physics

An International Journal at the Interface Between Chemistry and Physics

ISSN: (Print) (Online) Journal homepage: https://www.tandfonline.com/loi/tmph20

Local surface crystal structure fluctuation on Li, Na and Mg metal anodes

Ingeborg Treu Røe & Sondre Kvalvåg Schnell

To cite this article: Ingeborg Treu Røe & Sondre Kvalvåg Schnell (2022): Local surface crystal structure fluctuation on Li, Na and Mg metal anodes, Molecular Physics, DOI: 10.1080/00268976.2022.2053217

To link to this article: https://doi.org/10.1080/00268976.2022.2053217

© 2022 The Author(s). Published by Informa UK Limited, trading as Taylor & Francis Group.

View supplementary material

Published online: 23 Mar 2022.

Submit your article to this journal

Article views: 47

View related articles

View Crossmark data

Full Terms & Conditions of access and use can be found at
https://www.tandfonline.com/action/journalInformation?journalCode=tmph20

MOLECULAR PHYSICS e2053217
https://doi.org/10.1080/00268976.2022.2053217

Taylor & Francis
Taylor & Francis Group

RESEARCH ARTICLE

OPEN ACCESS Check for updates

Local surface crystal structure fluctuation on Li, Na and Mg metal anodes

Ingeborg Treu Røe and Sondre Kvalvåg Schnell

Department of Materials Science and Engineering, Norwegian University of Science and Technology, Trondheim, Norway

ABSTRACT

Dendrite formation occurs on Li, Na, and Mg metal anodes in rechargeable batteries, and is a safety challenge, as well as a limiting factor for increasing energy- and power density. However, the behaviour of the dendrites differs depending on the anode material. In this study, we investigate the local bulk and surface crystal structure of Li, Na, and Mg surfaces to shed light on how differences in the morphology and structure of the anode surface and its metal deposits can explain differences in dendrite formation on Li, Na, and Mg anodes. The local bulk- and surface structure are found using molecular dynamics simulations in combination with the *surface adaptive common neighbour analysis*, and indicate that Li and Na surfaces are more prone to surface instabilities and formation of protrusions than Mg surfaces, which remain flat and hexagonal close-packed even near room temperature. Additionally, the equilibrium shapes of the Mg deposits obtained from density functional theory assume more flat and hexagonal shapes than the Li and Na deposits. Together, these results shed light on atomic mechanisms that may contribute to the different propensities of Li, Na, and Mg metal anodes to form dendrites.

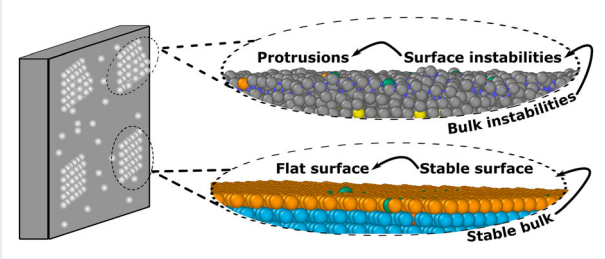

ARTICLE HISTORY
Received 25 August 2021
Accepted 28 January 2022

KEYWORDS
solid-state battery; molecular dynamics; solid-state physics

1. Introduction

Dendrite formation on the metal anode is a challenge in all-solid-state batteries, which prevents widespread commercialisation of such high-energy-density batteries [1]. Dendrites are tree-like structures that grow on the anode surface upon cycling of the battery. They deteriorate the anode and eventually short-circuit the battery. Additionally, moss- or whisker-like deposits can form on the anode during cycling causing a reduction in specific capacity and Coulombic efficiency [2–4]. For simplicity, we term all inhomogeneous deposits dendrites herein.

Dendrite formation is controlled by multiple factors. The current density influences both the on-set and morphology of the dendrites [5–9]. The composition of the electrolyte can determine the properties of the solid electrolyte interphase (SEI) which may direct metal deposition and suppress or enhance dendrite formation [10–13]. Similarly, additives in the electrolyte can adsorb on the anode surface and guide the deposition onto the anode [12,14,15]. Additionally, the surface texture of the current collector and anode have an impact [16–20]. However, neither of these factors can fully rationalise why different metal anodes show varying propensity to form dendrites. Mg anodes were, for example, long believed to not exhibit dendrite formation since the on-set current density is higher than that of Li [21,22]. Furthermore, the morphology of the dendrites are different in equivalent electrochemical environments for three promising metal anodes; Li, Na, and Mg [23,24].

CONTACT Sondre Kvalvåg Schnell sondre.k.schnell@ntnu.no

Supplemental data for this article can be accessed here. https://doi.org/10.1080/00268976.2022.2053217

© 2022 The Author(s). Published by Informa UK Limited, trading as Taylor & Francis Group.
This is an Open Access article distributed under the terms of the Creative Commons Attribution License (http://creativecommons.org/licenses/by/4.0/), which permits unrestricted use, distribution, and reproduction in any medium, provided the original work is properly cited.

The different mechanisms of dendrite formation on Li, Na and Mg metal anodes suggest that properties of the metals underlies these mechanisms. One such property is the crystal structure; Li and Na crystallize in the bcc structure while Mg crystallizes in the hcp at room temperature. The crystal structure affects the mobility of atoms adsorbed on the surface, *adatoms*, and the subsequent surface structure, which can influence the dendrite formation [21,25,26]. Together with the applied potential and the chemical environment, the crystal structure of the anode also determines the equilibrium shape of deposits on the Li, Na and Mg surface [27].

The equilibrium shape, or Wulff construction [28], minimises the surface energy of the deposit by organising the facets belonging to its bulk crystal structure such that the facets with the lowest surface energies dominate. In other words, the bulk crystal structure provides the boundaries of the Wulff construction, resulting in differences between the shapes of Li and Na in their bcc bulk crystal structure on one hand, and Mg in its hcp structure on the other. The surface energies of these allowed facets are determined by the properties of the elements, as well as the electrochemical environment. For Li, Na and Mg, the Wulff constructions have been successfully used to predict the morphology of the dendrites as the applied potential varies [29]. However, the prediction does not account for local fluctuations in the surface crystal structure of the anode. The substrate surface structure can affect the bulk crystal structure of the deposits through epitaxial growth, which may impact the morphology of the dendrites.

In the present work, we therefore study the local surface crystal structure of Li, Na, and Mg surfaces using molecular dynamics (MD) simulations in combination with the *surface adaptive common neighbour analysis* (saCNA) [30]. The local surface crystal structure is interpreted in relation to the equilibrium shapes of the metal single crystals with varying bulk crystal structures at 0 K, obtained from surface energy calculations using density functional theory (DFT) and the Wulff construction method. We find that Mg exhibits higher structural stability in its hcp bulk and surface structure at temperatures approaching room temperature than Li and Na in their bcc structures. Consequently, the Mg deposits will to a large degree adopt the hcp single-crystal equilibrium shape; a hexagonal platelet. In contrast, the shapes of Li and Na deposits vary owing to the less stable surface crystal structure. This can lead to enhanced fractal deposition on the Li and Na anodes compared to Mg. In addition, both clusters and protrusions observed to form on the Li and Na surfaces above 0 K, resulting in higher surface roughness than on the Mg surfaces, which may further enhance the formation of dendrites on the Li and Na anodes compared to Mg.

2. Computational methods

2.1. Density functional theory calculations

The Wulff constructions of Li, Na and Mg in the bcc, fcc and hcp structures were obtained using WulffPack [31]. All Wulff constructions contained 5000 atoms. Both the surface area and volume of a construction is found with Wulffpack, and the surface-to-volume ratio calculated as:

$$\frac{N_A}{N_V} = \frac{4Ar}{3V}, \tag{1}$$

where A is the surface area, r is the atomic radius and V is the volume. The low-Miller-index surface energies input to Wulffpack were calculated with the density functional theory (DFT) software Vienna *Ab initio* Simulation Package (VASP) [32,33]. The calculations were performed with the PBEsol functional [34] and the projector augmented wave pseudopotentials, which included the s, sp and spd core electrons and were expanded to 500 eV, 350 eV and 350 eV for Li, Na, and Mg, respectively. The bulk simulation cells of all elements in the bcc, fcc and hcp structures were relaxed with respect to the cell volume and shape, and the ion positions. The resulting lattice constants are exhibited in Table S1. The bulk energy was calculated for the relaxed bulk simulation cell, and its lattice constant was used to create the surface simulation cells.

The surface simulation cells exceeded 14 Å in all directions, plus a vacuum of more than 15 Å in the direction perpendicular to the surface (*i.e.* z-direction). The four uppermost layers in the z-direction were free to move while the rest of the atoms were fixed in space to mimic the bulk. The maximum force on all bulk and surface simulation cells were relaxed to within 0.001 eV/ Å, but only the atomic positions were allowed to relax in the surface simulation cells (*i.e.* the shape and volume were fixed). The surface energy is calculated according to Equation S1. Based on the surface energies of one element within a crystal structure, the surface ratio is defined as:

$$r_{crystal} = \frac{\gamma_{crystal}}{\gamma^{hi}_{crystal}}, \tag{2}$$

where $\gamma_{crystal}$ is the surface energy of one of the facets belonging to a specific crystal structure, and $\gamma^{hi}_{crystal}$ is the facet with the highest surface energy belonging to the same crystal structure. Further details on the bulk and surface DFT calculations are found in the Supplementary Information (SI).

2.2. Molecular dynamics simulations

Molecular dynamics (MD) simulations were performed using the Large-scale Atomic/Molecular Massively Parallel Simulator (LAMMPS) [35] with MEAM-potentials [36] for Li, Na and Mg. The lattice constants of Li, Na and Mg in the bcc, bcc and hcp structures, respectively, predicted using the MEAM-potentials are in agreement with experimental and computational literature. The potentials are therefore assumed to adequately predict the crystal structures of Li, Na and Mg surfaces. The obtained lattice constants are given in Table S2 in the SI together with details on the lattice constant simulations. The melting points of Li, Na and Mg predicted with the MEAM-potentials, were 273 K and 500 K, respectively. While these are 98 K and 423 K lower than the experimental melting points, the simulation routine used to find the melting points, described in the SI, are associated with large uncertainties [37]. Yet, we restrict the crystal structure analyses to below 200 K for Li and Mg and below 150 K for Na to ensure that the simulations of the surfaces are performed away from the melting points.

The simulations of the Li, Na and Mg surfaces were performed in the canonical (NVT) ensemble with the Nose-Hoover thermostat for temperatures of 10 K, 50 K, 150 K and 200 K. The simulation cells were initiated in the bcc, fcc and hcp bulk structures with their respective 0 K lattice constant and a vacuum of minimum 100 Å in the direction perpendicular to the surface (*i.e.* z-direction). The cell geometry in the x- and y-direction was allowed to relax in the NPT ensemble at the given temperature and 1 atm isostatic pressure for 1 ns. The average lattice constants over the last 0.1 ns of the NPT simulation was used in the subsequent NVT simulation. The NVT simulations were ran for 1 ns with 0.1 ps thermostat relaxing time. Position data was sampled every 1.0 ps. The surface adaptive common neighbour analysis (sa-CNA) was used to find the local bulk and surface crystal structures. In the sa-CNA, the surface atoms are the atoms constituting the uppermost layer of the simulation cell, while the bulk atoms are the rest. The sa-CNA is introduced briefly in the SI, but was developed in [30], where further details can be found.

3. Results and discussion

3.1. Wulff constructions

Wulff constructions are indicative of the shape of a particle deposited in a surface. The Wulff constructions are influenced by the bulk crystal structure of the particle, which is also impacted by the crystal structure of the surface onto which the particle is deposited. To investigate the impact of varying bulk crystal structures on the shapes of the respective metal deposits, we created Wulff constructions for Li, Na, and Mg in the bcc, fcc and hcp bulk crystal structures based on the low-Miller-index surface energies belonging to the various crystal structures. The surface energies are presented in Table S2. Figure 1 depicts the resulting single crystal Wulff construction of Li, Na, and Mg in the bcc, fcc, and hcp structures together with the surface-to-volume ratios calculated according to Equation (1). The Wulff constructions are oriented with the lowest energy surface in the xy-plane. The surface-to-volume ratio indicates the shape of the construction since a higher ratio implies a flatter shape. Figure 1 shows a 2–3% increase in surface-to-volume ratio from bcc to hcp for all of the elements, implying that the hcp constructions are flatter than the bcc. Furthermore is the increase at 2–6% from Li to Mg regardless of the underlying bulk crystal structure. This is indicative of flatter Mg compared to Li and Na constructions, and implies that Mg metal deposits are flatter than Li and Na even if the crystal structure of the surface, onto which the metal is deposited, deviates from the room temperature bulk crystal structure of the metal. This is consistent with the hexagonal platelet shape observed experimentally for Mg deposits [23], and may help explaining why Mg is less prone to fractal deposition and dendrite formation than Li and Na.

The Wulff constructions are determined by the surface energies of the facets, as well as the underlying bulk crystal structure. A flat construction is therefore caused partly by a low surface energy of a single facet compared to the other facets. The surface ratio, defined in Equation (2), describes how much a specific facet dominates. The surface ratios of the Li, Na and Mg bcc, fcc and hcp facets are given in Table 1, and shows that within each of the bulk crystal structures, there is one Mg facet that has significantly lower surface energy than the other facets, while both for Li and Na, the facets exhibit more similar surface energies. This suggests that the flatter shapes observed for Mg metal deposition compared to Li and Na deposition arise from the relatively lower surface energy of one Mg facet, and that this trend is insensitive to the crystal structure of the surface onto which the metals are deposited.

In Table 1 the DFT calculated bulk energies of Li, Na and Mg in the bcc, fcc and hcp structures are shown, together with the corresponding surface ratios. The simulations show that Li and Na are most stable in the close-packed structures at 0 K. We note that this agrees with the observed phase transition from the fcc and faulted hcp structures at 78 K and 32 K for Li and Na, respectively [38–40]. Entropic contributions at increasing temperatures are given as the driving force for the phase transitions, and the lower transition temperature

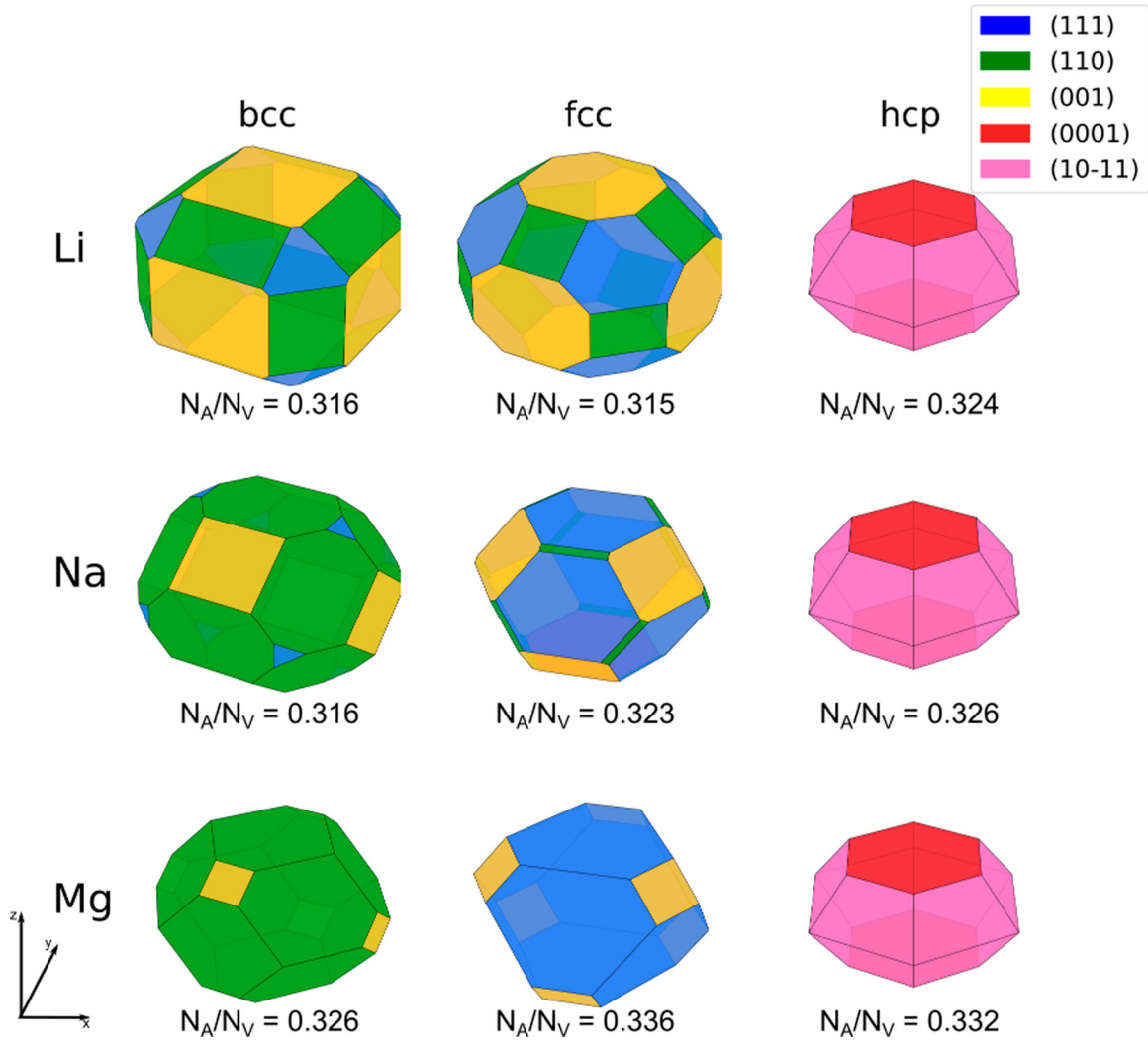

Figure 1. The Wulff constructions of (top row) Li, (middle row) Na and (bottom row) Mg in (left column) bcc, (middle column) fcc and (right column) hcp. The Wulff constructions are created with the surface energies from Table S2.

Table 1. Bulk energies (*eV/atom*) and surface ratio for Li, Na and Mg in the bcc, fcc and hcp crystal structure. The surface ratio is defined according Equation (2).

		bcc			fcc			hcp	
Energy	Element	001	110	111	001	110	111	0001	10–11
Bulk (*eV/atom*)	Li		−1.963			−1.968			−1.968
	Na		−1.397			−1.397			−1.399
	Mg		−1.693			−1.709			−1.721
Surface ratio	Li	0.841	0.927	1.000	0.911	1.000	0.963	0.868	1.000
	Na	0.878	0.859	1.000	0.910	1.000	0.840	0.825	1.000
	Mg	0.921	0.771	1.000	0.994	1.000	0.776	0.774	1.000

of Na compared to Li may be explained by the more similar bulk energies of the bcc, fcc and hcp structures at 0 K of Na compared to Li, which also suggests that Na is more stable in its bcc bulk crystal structure at room temperature than Li. The stability of the bulk may affect the stability of the surface. Consequently, Na deposits might take on the shape of the bcc Wulff construction in Figure 1 to a larger extent than Li. Surface crystal structure stability can facilitate less fractal growth of the deposits on the surface since the shapes of the deposits are more homogeneous. This notion needs, however, further investigation on time and space scales that cover both the micro- and macroscopic dimensions simultaneously.

The Wulff constructions of Li, Na and Mg in the bcc, fcc and hcp crystal structures shows that, overall, the Mg single crystals exhibit flatter shapes than the Li and Na. Thus, Mg metal deposits may assume

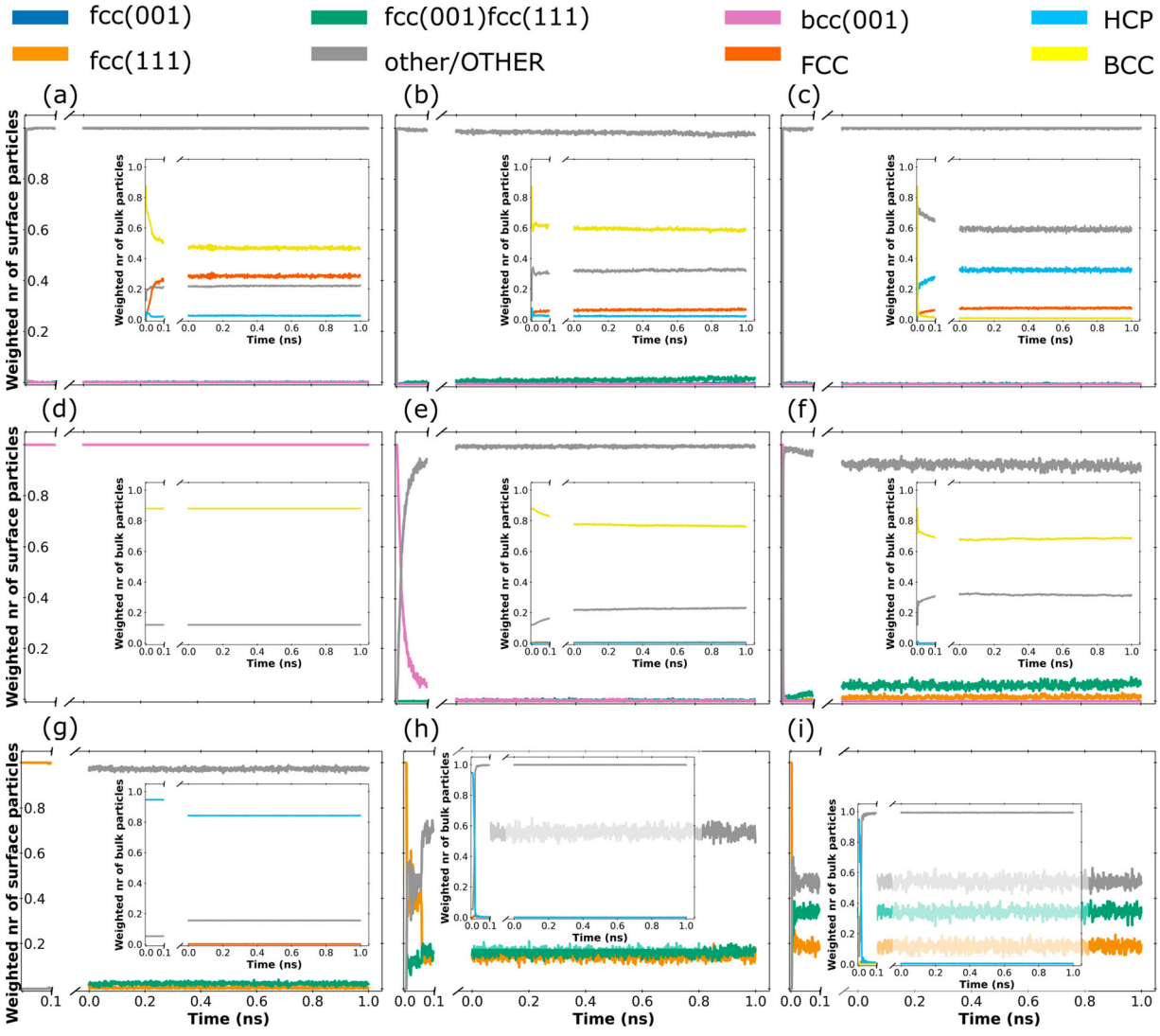

Figure 2. The surface crystal structure of Li ((a–c)), Na ((d–f)) and Mg ((g–i)) at 10 K ((a,d) and (g)), 50 K ((b,e) and (h)) and 200 K ((c) and (i); 150 K in (f)). The insets shows the bulk crystal structure. Li, Na and Mg are initiated in the bcc, bcc, and hcp crystal structures, respectively. The lowercase labels are surface crystal structure while the uppercase labels are bulk crystal structure.

a flatter shape than the Li and Na deposits even when the crystal structure varies across the surface onto which the metal is deposited. The flatter shapes of the Mg Wulff constructions can reduce Mg's tendency to form dendrites compared to Li and Na, and arise from the dominance in surface energy of one single facet. Consequently, one way to reduce the dendrite formation on Li and Na surfaces may be to reduce the surface energy of specific facets.

3.2. Local surface crystal structure

Fluctuations in the bulk and surface crystal structure can affect the morphology of deposits on the surface. To investigate the extent of both bulk and surface crystal structure fluctuations in Li, Na and Mg metals, we performed a surface adaptive common neighbour analysis (sa-CNA) on Li, Na and Mg surfaces obtained from molecular dynamics (MD) simulations at 10 K, 50 K, and 150 K for Na and 200 K for Li and Mg. The weighted number of surface and bulk particles (*i.e.* the number of atoms in a specific surface or bulk crystal structure over the total amount of surface or bulk atoms) are shown in Figure 2 (the bulk crystal structures are shown in the insets). The uppercase labels are bulk whereas the lowercase are surface crystal structures. In the present work, the detectable surface structures are fcc(001), fcc(111), fcc(111) on a fcc(001) substrate and bcc(001). The corresponding labels are fcc(001), fcc(111), fcc(001)fcc(111) and bcc(001). Notice that the fcc(111) is equivalent to the hcp(0001) surface. Also note that the binary surfaces presented herein are not the only possible surfaces. Since each surface must be identified and characterised in the sa-CNA (see the SI), the number of detected surfaces is

limited. The first 0.1 ns after the simulation is initiated is shown before the break in the x-axis (*i.e.* the structure evolution from the 0 K lattice).

The simulation cells are initiated in the room temperature crystal structures, meaning the bcc for Li and Na and the hcp structure for Mg. Figure 2(a) shows that Li does not retain its bcc surface structure at 10 K. This is not surprising as Li is more stable in the fcc bulk structure at temperatures close to 0 K [38], as seen in Table 1. Furthermore, it is consistent with the inset of Figure 2(a) showing a partial transformation from the bcc to the fcc bulk crystal structure, indicating that the bulk instabilities cause the surface instabilities and restructuring away from the bcc surface structure. As a side note, the Li simulation cell initiated in the fcc bulk structure fully retains its surface fcc (001) and partly its bulk fcc structure, as depicted in Figure 3, in accordance with the fcc bulk structure observed to be more stable close to 0 K. Although the bcc bulk structure is more dominant at 50 K as shown in the inset of Figure 2(b), the amount of unrecognised bulk atoms increases. Thus, the bulk crystal instabilities of Li still propagates to the surface and render the surface crystal structure unrecognised.

Figure 2(d) shows that the bcc bulk and surface crystal structure of Na is retained at 10 K. This is attributed to the fact that although Na experience a phase transformation from hcp to bcc similar to Li [39], the phase transition temperature is lower than for Li owing to the small difference between the 0 K bulk energies of Na hcp and bcc shown in Table 1. Hence, the bcc structure is more likely to be meta stable for Na at 10 K than it is for Li. Additionally, the higher stability of the Na bcc structure is confirmed by the higher ratio of bcc bulk atoms in the Na compared to the Li simulation cells at 50 K and 150 K/200 K Figure 2(b,c,e) and (f). This may lead to the stabilised bcc surface at 10 K Figure 2(d), and the slightly slower transition of the surface from the bcc structure at 50 K and 150 K. All the same, sa-CNA reveals that the Na surfaces are unstable in their bcc surface structure at temperatures approaching room temperature, indicating that only small bulk instabilities may cause surface instabilities. However, this may also suggest that additional factors to the bulk structure contributes to the surface crystal structure stability.

Surprisingly, the Mg surface structure in Figure 2(g) is not recognised although the hcp bulk crystal structure is retained. Upon visual inspection, the deviation from the hcp surface structure is caused by a coordinated translation of the surface from the hollow hcp positions to a top/bridge position. The translation is illustrated in Figure 4, and represents a stacking fault. We investigated the stability of this stacking fault at 0 K using DFT, and revealed that the top position is meta stable, but with a seven times higher surface energy. The DFT results therefore suggest an underestimation of the stacking fault energy in the Mg MEAM potentials used herein, which allows the stacking fault to occur. This notion is confirmed by the MD simulations at 50 K and 200 K, where multiple stacking faults along the z-direction of the simulation cells cause the bulk structure to transition from the hcp to an unrecognised structure, as shown in Figure 2(h) and (i).

Due to the stacking faults of the Mg simulation cells that render the surface unrecognisable, it is challenging to conclude on the degree of surface crystal structure fluctuation in the Mg surfaces at elevated temperatures. However, the increasing amount of close-packed surface structures (fcc(111) and fcc(001)fcc(111)) in Figure 2(h) and (i) suggests a hexagonal surface. Additionally, visual inspection indicates the same. Figure 5 depicts the Mg surface layer and the four uppermost substrate layers after 0.5 ns at 10 K and 200 K. The surface atoms closer than 3.4 Å, which is the interatomic distance between the nearest neighbours in the initial hcp structure, are shown as bonded. Figure 5 shows a complete and nearly-complete bonding of all surface atoms in one layer at 10 K and 200 K, indicating that the surface is flat and hexagonal close-packed. Similarly, the bulk is not recognised as hcp stacking faults even though the layers in the bulk are flat and hexagonal close-packed. We attribute this to the underestimation of the stacking fault energy of the Mg MEAM potential, suggesting that the hcp surface and bulk structure is stable at these elevated temperatures.

In contrast, the mechanism for the transition to unrecognisable structures for the Li surface at 10 K is different. Figure 6 depicts the Li surface layer and the four uppermost substrate layers after 0.5 ns at 10 K and 200 K. The surface atoms closer than 3.20 Å, which is the interatomic distance between nearest neighbours in the initial bcc structure, are shown as bonded. Even though the surface atoms are not bonded in the initial configuration, Figure 6 illustrates how the surface atoms group together in couples or chains. At 10 K, the grouping is synchronised and the surface atoms create a pattern while at 200 K, the surface atoms start forming clusters. The clustering is associated with slight protrusions as illustrated in the side view in Figure 6(b). Such protrusions enhance dendrite formation especially when combined with an excess charge in the surface [9].

Although Na exhibits higher stability in its bcc surface structure at 10 K, the surface quickly collapses to an unrecognised structure at 50 K and 150 K. Figure 7 shows the top and side view of the Na surface and the four uppermost substrate layers at 50 K and 150 K. The

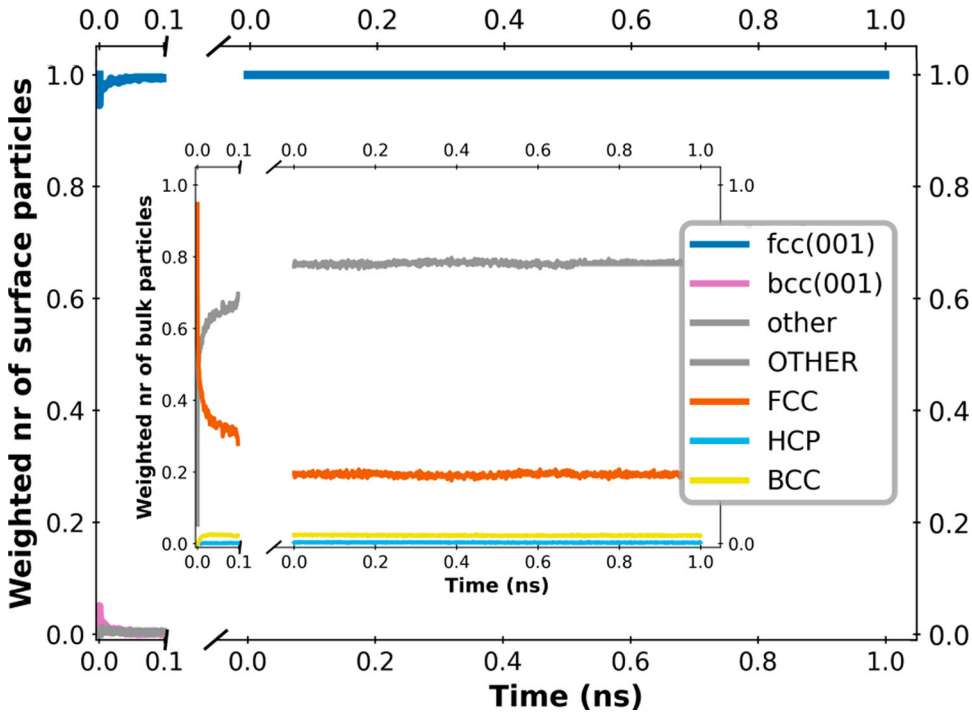

Figure 3. The surface crystal structure of Li initiated in the fcc structure at 10 K. The bulk crystal structure is shown in the inset.

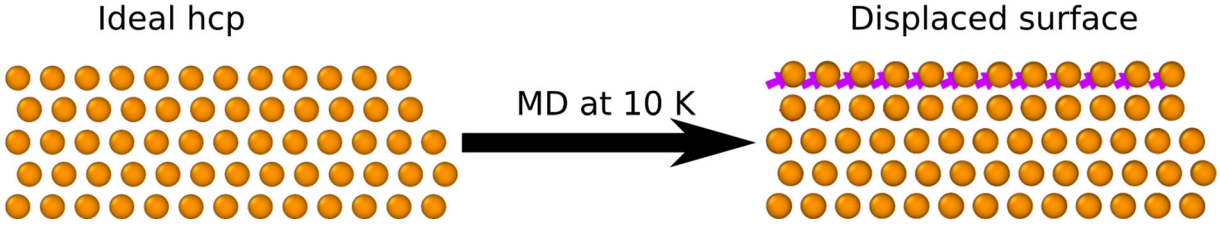

Figure 4. Illustration of the translation of the Mg surface to a top/bridge position after 0.5 ns at 10 K. The purple arrows are displacement vectors showing the displacements of the atoms from their position in the initial 0 K Mg hcp structure (left). The Mg atoms are coloured orange, and drawn with 1 Å radius to clearly see the displacement vectors.

surface atoms closer than 4.00 Å, which is the interatomic distance between nearest neighbours in the initial bcc structure, are shown as bonded. Compared to the Li surfaces in Figure 6, the Na surfaces do not form a pattern to the same extent, but exhibit an even larger tendency to form clusters and protrusions than Li.

Due to the limited number of surfaces detected in the sa-CNA, there may be surface structures omitted in the analysis, resulting in seemingly more disordered surfaces than they are in reality. On the other hand, Figure 6 and 7 show a degree of disorder on the Li and Na surfaces making detection of other Li and Na surface structures unlikely, whereas the close-packed surface structure of Mg is detected, excluding other Mg surface structures. Moreover, the sa-CNA performed in the present work support the DFT calculations of the bulk energies suggesting that the bulk crystal structures of Na and Mg are more stable than that of Li. Hence, the sa-CNA indicates that the instabilities in the bulk structure propagates to the surface structure, and makes the Li surfaces prone to formation of clusters and protrusions. Clusters and protrusions also form on Na surfaces even though the bulk structure is more stable than that of Li. The clusters and protrusions can act as nucleation centres for dendrite formation and generate inhomogeneous deposition on the Li and Na surfaces at 200 K and 150 K. In contrast, the Mg surfaces remains flat even at these temperatures, and may therefore be less susceptible to dendrite formation than Li and Na anodes.

Although the trends shown in this study are indicative of the behaviour of Li, Na and Mg surfaces in batteries, the temperatures are limited by the MEAM potentials

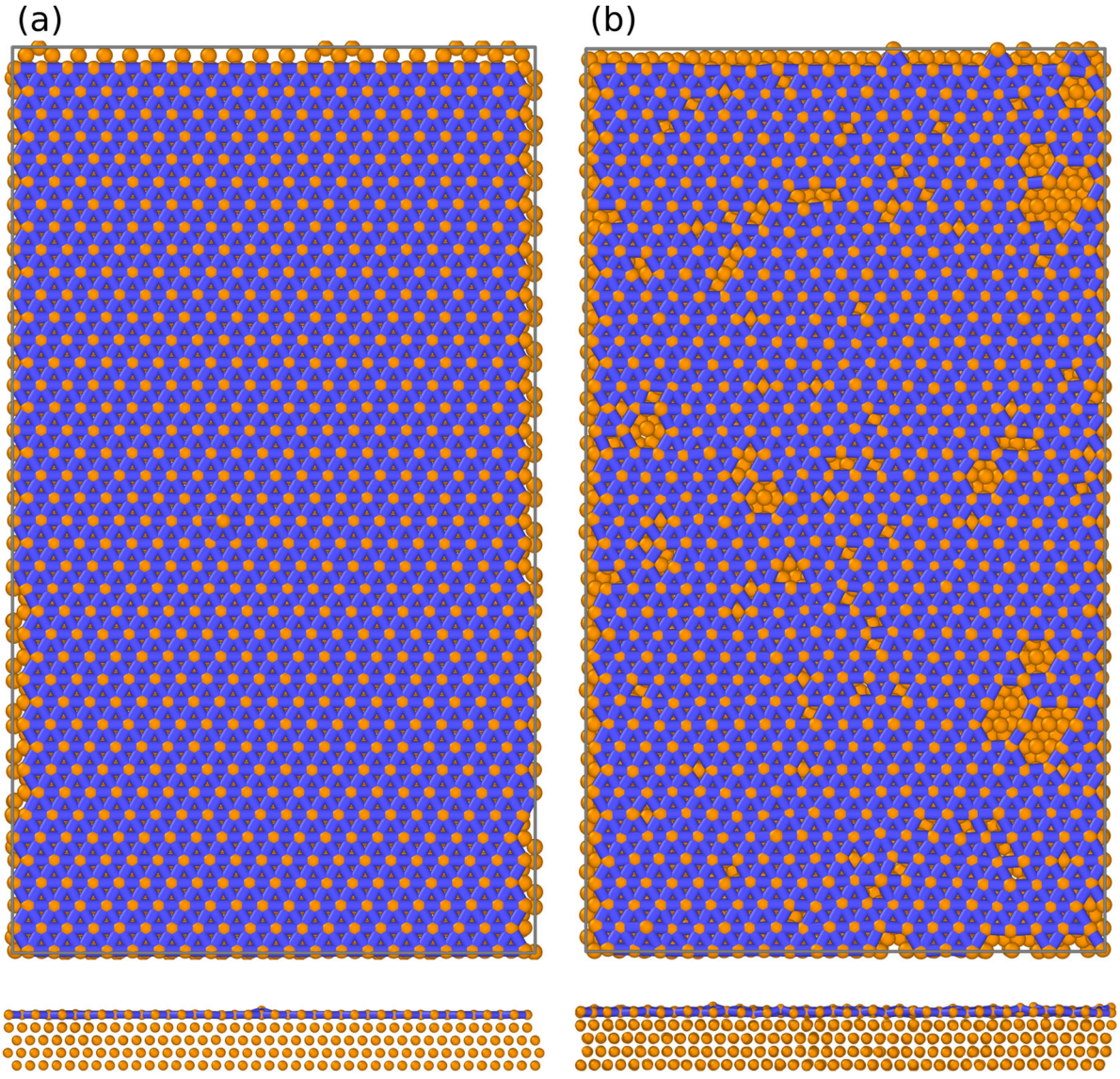

Figure 5. Illustration of the bonding of the Mg atoms into flat, hexagonal close-packed surfaces after 0.5 ns at (a) 10 K and (b) 200 K. Top and side view shown in the upper and lower panes, respectively. Surface atoms closer than 3.4 Å are shown as bonded (blue bond). The Mg atoms are coloured orange, and are drawn with 1 Å radius to clearly see the bonds.

used herein, and do not reach realistic operating temperatures at around 300 K. Increasing temperatures increases the motion of the atoms. This increase is related to the Arrhenius equation:

$$k = \nu \cdot \exp\left(-\frac{E_b}{k_B T}\right), \tag{3}$$

where ν is the attempt frequency, E_b is the energy barrier for the motion, k_B is the Boltzmann constant and T is the temperature. Depending on the type of motion, the energy barrier is different. The energy barriers of surface diffusion, known from DFT calculations [26,41], is approximately twice as large for Li and Na compared to Mg, whose energy barrier is on the order of the thermal energy at room temperature, $k_B T = 25$ meV. For the interaction energy between the nearest neighbours in a surface layer, the situation is turned around, with Mg having around twice as large interaction energy than Li and Na [42]. Consequently, as the temperature increases towards room temperature, Li and Na atoms are excited more easily from their ideal position in the surface layer, while the Mg interaction energy remains high compared to the thermal energy. Simultaneously will the ability of excited Mg atoms to fall back into their ideal surface positions be higher because the surface diffusion is fast. The surface diffusion of Li and Na remain comparatively slow because the energy barrier is larger than the thermal energy. In total, we therefore expect the trends shown in this study to hold even at realistic battery operating temperatures.

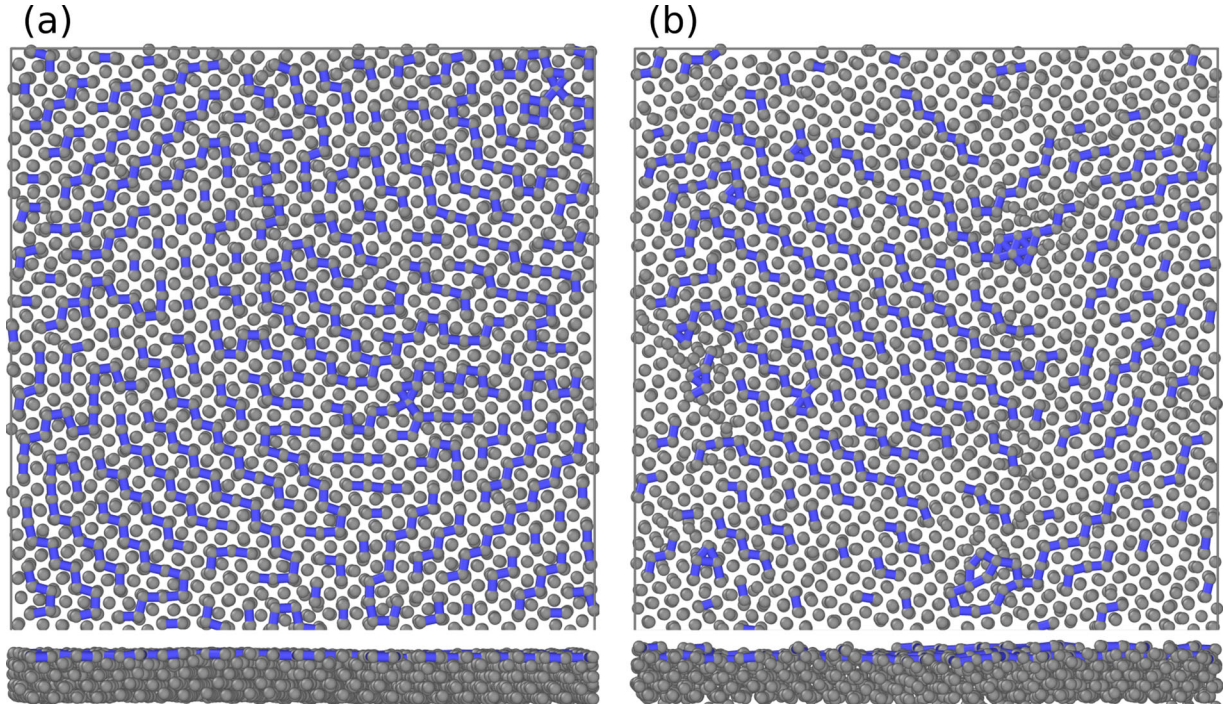

Figure 6. Illustration of the grouping of Li surface atoms into couples or chains after 0.5 ns at (a) 10 K and (b) 200 K. Top and side view shown in the upper and lower panes, respectively. Surface atoms closer than 3.20 Å and 3.26 Å are shown as bonded (blue bond). The Li atoms are coloured grey, and are drawn with 1 Å radius to clearly see the bonds.

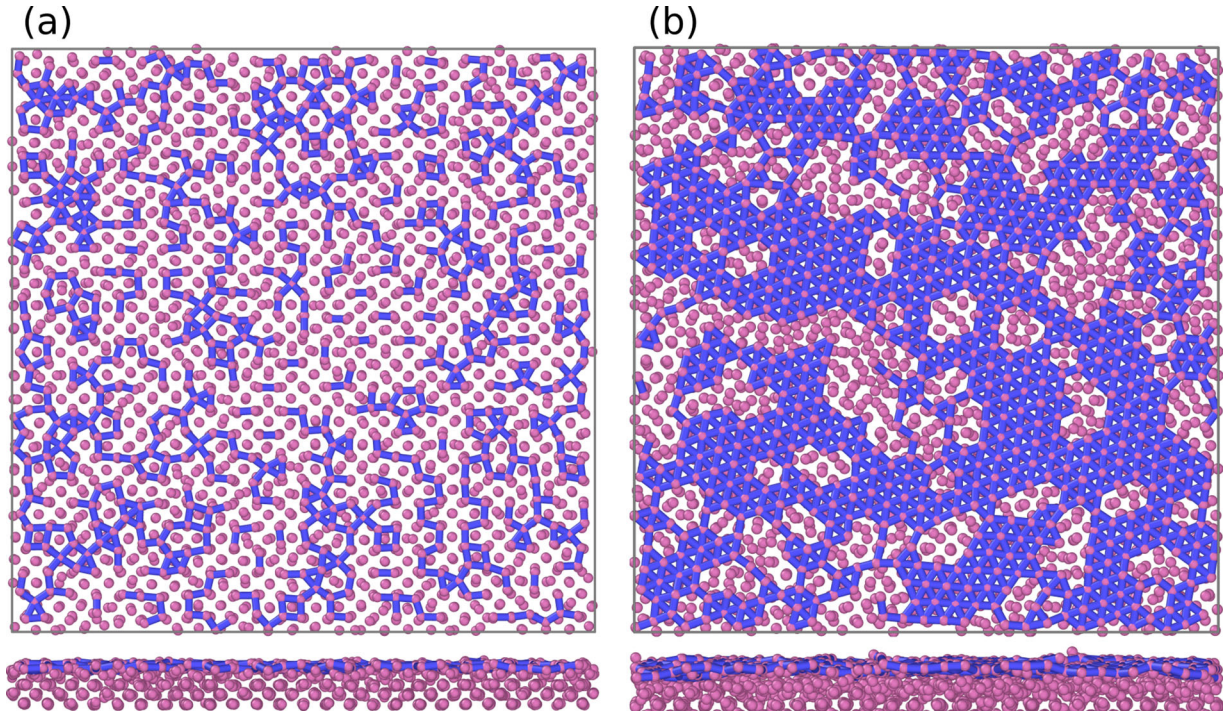

Figure 7. Illustration of the grouping of Na surface atoms into clusters after 0.5 ns at (a) 50 K and (b) 15 K. Top and side view shown in the upper and lower panes, respectively. Surface atoms closer than 4.00 Å are shown as bonded (blue bond). The Na atoms are coloured purple, and are drawn with 1 Å radius to clearly see the bonds.

4. Conclusions

In the present work, we have studied the local crystal structure of the alkali metals, Li and Na, and the earth-alkali metal Mg using a combination of density functional theory (DFT) and molecular dynamics (MD) simulations. The local bulk and surface crystal structures have been unravelled with the surface adaptive common neighbour analysis (sa-CNA), and have provided insights into the surface structure and morphology evolution of Li, Na, and Mg surface at temperatures approaching room temperature. Furthermore, the 0 K Wulff construction of Li, Na and Mg in the bcc, fcc and hcp bulk crystal structures are used to indicate how the shape of a deposit change with the surface crystal structure.

The sa-CNA combined with the DFT bulk energy calculations suggest that Na and Mg are more stable in the bcc and hcp bulk structure at room temperature than Li is in the bcc bulk structure. The instabilities of the Li bulk structure may propagate to the surface, and induce texturing and protrusions that can act as nucleation sites for dendrite formation. The Na surface atoms are found to cluster together and form protrusions as the temperature increases towards room temperature even though the bulk bcc structure is more stable than that of Li. The bulk crystal structure of Mg, on the other hand, remains hexagonal, and accordingly, the surface retains its flat and hexagonal close-packed structure even as the temperature approaches room temperature. Thus, there may be fewer nucleation sites for dendrite formation on Mg compared to Li and Na surfaces.

In addition, may the surface structure affect the shapes of the deposits on the surface. Thus, the smaller variation in crystal structure across the Mg compared to the Li and Na surfaces can lead to more homogeneous shapes of the deposits. Moreover, the Wulff constructions of Mg are found to be flatter than those of Li and Na, regardless of the underlying crystal structure, which may further enhance homogeneous deposition on the Mg surface. Consequently, we may understand the higher tendency to form dendrites on Li and Na compared to Mg metal anodes as a result of the interplay between the bulk and surface crystal structure stability and the shape of the deposits corresponding to the crystal structure of the surface. Furthermore, this highlights a possible pathway towards reduced dendrite formation, where the surface is stabilised relative to all other possible facets, resulting in less surface instabilities and flatter shapes of the deposits.

Disclosure statement

No potential conflict of interest was reported by the author(s).

Funding

The author thanks Sigma2 for CPU time through the project NN9566K. The Faculty of Natural Sciences at Notur/Norstore (NTNU) is acknowledged for financial support.

Supporting information

Supporting Information (SI) including computational details for the DFT and MD simulations, and a brief description of the sa-CNA procedure is found at:

ORCID

Ingeborg Treu Røe http://orcid.org/0000-0003-1215-1255
Sondre Kvalvåg Schnell http://orcid.org/0000-0002-0664-6756

References

[1] D. Lin, Y. Liu and Y. Cui, Nat. Nanotechnol. **12** (3), 194–206 (2017). doi:10.1038/nnano.2017.16
[2] J. Xiao, Q. Li, Y. Bi, M. Cai, B. Dunn, T. Glossmann, J. Liu, T. Osaka, R. Sugiura, B. Wu, J. Yang, J.G. Zhang and M.S. Whittingham, Nature Energy **5**, 561–568 (2020 Aug). doi:10.1038/s41560-020-0648-z
[3] X. Liang, Q. Pang, I.R. Kochetkov, M.S. Sempere, H. Huang, X. Sun and L.F. Nazar, Nature Energy**2**, 17119 (2017 Jul). doi:10.1038/nenergy.2017.119
[4] C. Niu, H. Lee, S. Chen, Q. Li, J. Du, W. Xu, J.G. Zhang, M.S. Whittingham, J. Xiao and J. Liu, Nature Energy **4**, 551–559 (Jul 2019). doi:10.1038/s41560-019-0390-6
[5] I.W. Seong, C.H. Hong, B.K. Kim and W.Y. Yoon, J. Power. Sources. **178** (2), 769–773 (2008). doi:10.1016/j.jpowsour.2007.12.062
[6] R. Akolkar, J. Power. Sources. **232**, 23–28 (2013). doi:10.1016/j.jpowsour.2013.01.014
[7] D.R. Ely and R.E. Garcia, J. Electrochem. Soc. **160** (4), A662–A668 (2013). doi:10.1149/1.057304jes
[8] X. Xu, Y. Liu, J. Hwang, O.O. Kapitanova, Z. Song, Y. Sun, A. Matic and S. Xiong, Adv. Energy. Mater. **11**, 2002390 (Oct 2020). doi:10.1002/aenm.v10.44
[9] E. Santos and W. Schmickler, Angewandte Chemie International Edition **60**, 5876–5881 (Mar 2021). doi:10.1002/anie.v60.11
[10] A.C. Kozen, C.-F. Lin, A.J. Pearse, M.A. Schroeder, X. Han, L. Hu, S.-B. Lee, G.W. Rubloff and M. Noked, ACS. Nano. **9**, 5884–5892 (Jun 2015). doi:10.1021/acsnano.5b02166
[11] H. Wang, M. Matsui, H. Kuwata, H. Sonoki, Y. Matsuda, X. Shang, Y. Takeda, O. Yamamoto and N. Imanishi, Nat. Commun. **8** (1), 1–9 (2017). doi:10.1038/s41467-016-0009-6
[12] J. Zheng, M.H. Engelhard, D. Mei, S. Jiao, B.J. Polzin, J.G. Zhang and W. Xu, Nature Energy **2**, 17012 (2017). doi:10.1038/nenergy.2017.12
[13] E. Cha, M.D. Patel, J. Park, J. Hwang, V. Prasad, K. Cho and W. Choi, Nat. Nanotechnol. **13** (4), 337–344 (2018). doi:10.1038/s41565-018-0061-y
[14] F. Ding, W. Xu, X. Chen, J. Zhang, Y. Shao, M.H. Engelhard, Y. Zhang, T.A. Blake, G.L. Graff, X. Liu and

J.G. Zhang, Journal of Physical Chemistry C **118** (8), 4043–4049 (2014). doi:10.1021/jp4127754
[15] Y. Lu, Z. Tu and L.A. Archer, Nat. Mater. **13**, 961–969 (2014). doi:10.1038/nmat4041
[16] G. Zheng, S.W. Lee, Z. Liang, H.-W. Lee, K. Yan, H. Yao, H. Wang, W. Li, S. Chu and Y. Cui, Nat. Nanotechnol. **9** (8), 618–623 (2014). doi:10.1038/nnano.2014.152
[17] M.-H. Ryou, Y.M. Lee, Y. Lee, M. Winter and P. Bieker, Adv. Funct. Mater. **25**, 834–841 (Feb 2015). doi:10.1002/adfm.201402953
[18] X. Wang, W. Zeng, L. Hong, W. Xu, H. Yang, F. Wang, H. Duan, M. Tang and H. Jiang, Nature Energy **3**, 227–235 (Mar 2018). doi:10.1038/s41560-018-0104-5
[19] X. Chen, X.R. Chen, T.Z. Hou, B.Q. Li, X.B. Cheng, R. Zhang and Q. Zhang, Sci. Adv. **5**, eaau7728 (Feb 2019). doi:10.1126/sciadv.aau7728
[20] X. Ma, X. Chen, Y. Bai, X. Shen, R. Zhang and Q. Zhang, Small **17**, 2007142 (Dec 2021). doi:10.1002/smll.v17.48
[21] J. Steiger, G. Richter, M. Wenk, D. Kramer and R. Mönig, Electrochem. Commun. **50**, 11–14 (2015). doi:10.1016/j.elecom.2014.11.002
[22] M. Matsui, J. Power. Sources. **196**, 7048–7055 (2010). doi:10.1016/j.jpowsour.2010.11.141
[23] R. Davidson, A. Verma, D. Santos, F. Hao, C. Fincher, D. Zhao, V. Attari, P. Schofield, J. Van Buskirk, A. Fraticelli-Cartagena, T. Alivio, R. Arroyave, K. Xie, M. Pharr, P. Mukherjee and S. Banerjee, Materials Horizon **7** (3), 843–854 (2020). doi:10.1039/C9MH01367A
[24] Y. Gu, W.W. Wang, Y.J. Li, Q.H. Wu, S. Tang, J.W. Yan, M.S. Zheng, D.Y. Wu, C.H. Fan, W.Q. Hu, Z.B. Chen, Y. Fang, Q.H. Zhang, Q.F. Dong and B.W. Mao, Nat. Commun. **9**, 1–9 (Dec 2018). doi:10.1038/s41467-017-02088-w
[25] K.J. Harry, D.T. Hallinan, D.Y. Parkinson, A.A. Macdowell and N.P. Balsara, Nat. Mater. **13** (1), 69–73 (2013). doi:10.1038/nmat3793
[26] I.T. Røe, S.M. Selbach and S.K. Schnell, Journal of Physical Chemistry Letters **11**, 2891–2895 (Apr 2020). doi:10.1021/acs.jpclett.0c00819
[27] A. Hagopian, D. Kopač, J.-S. Filhol and A.K. Lautar, Electrochim. Acta. **353**, 136493 (May 2020). doi:10.1016/j.electacta.2020.136493
[28] G. Wulff, Zeitschrift Für Kristallographie – Crystalline Materials **34**, 449–530 (Jan 2014). doi:10.1524/zkri.1901.34.1.449
[29] A. Hagopian, M.L. Doublet and J.S. Filhol, Energy and Environmental Science **13**, 5186–5197 (Dec 2020). doi:10.1039/D0EE02665D
[30] I.T. Røe and S.K. Schnell, Journal of Materials Chemistry A **9**, 11044–11048 (2021). doi:10.1039/D1TA02300D.
[31] J. Rahm and P. Erhart, Journal of Open Source Software **5**, 1944 (Jan 2020). doi:10.21105/joss
[32] G. Kresse and J. Furthmüller, Computational Materials Science **6**, 15–50 (Jul 1996). doi:10.1016/0927-0256(96)00008-0
[33] G. Kresse and D. Joubert, Phys. Rev. B. **59**, 1758–1775 (Jan 1999). doi:10.1103/PhysRevB.59.1758
[34] J.P. Perdew, A. Ruzsinszky, G.I. Csonka, O.A. Vydrov, G.E. Scuseria, L.A. Constantin, X. Zhou and K. Burke, Phys. Rev. Lett. **100**, 136406 (2008). doi:10.1103/PhysRevLett.100.136406
[35] S. Plimpton, J. Comput. Phys. **117**, 1–19 (Mar 1995). doi:10.1006/jcph.1995.1039
[36] M.I. Baskes, Phys. Rev. B. **46**, 2727–2742 (Aug 1992). doi:10.1103/PhysRevB.46.2727
[37] Y. Zhang and E.J. Maginn, J. Chem. Phys. **136**, 144116 (2012). doi:10.1063/1.3702587
[38] G.J. Ackland, M. Dunuwille, M. Martinez-Canales, I. Loa, R. Zhang, S. Sinogeikin, W. Cai and S. Deemyad, Science (New York, N.Y.) **356**, 1254–1259 (Jun 2017). doi:10.1126/science.aal4886
[39] R. Berliner, H.G. Smith, J.R. Copley and J. Trivisonno, Phys. Rev. B. **46**, 14436–14447 (Dec 1992). doi:10.1103/PhysRevB.46.14436
[40] W. Schwarz, O. Blaschko and I. Gorgas, Phys. Rev. B. **46**, 14448–14452 (Dec 1992). doi:10.1103/PhysRevB.46.14448
[41] D. Gaissmaier, M. Borg, D. Fantauzzi and T. Jacob, ChemSusChem **13**, 1–14 (Jan 2020). doi:10.1002/cssc.v13.4
[42] M. Jäckle and A. Groß, J. Chem. Phys. **141**, 174710 (Nov 2014). doi:10.1063/1.4901055